Available online at www.sciencedirect.com
ScienceDirect
Journal of Computational Physics 226 (2007) 2078–2095
JOURNAL OF COMPUTATIONAL PHYSICS
www.elsevier.com/locate/jcp

Diffuse interface model for incompressible two-phase flows with large density ratios

Hang Ding [a,*], Peter D.M. Spelt [a], Chang Shu [b]

[a] Department of Chemical Engineering, Imperial College London SW7 2AZ, UK
[b] Department of Mechanical Engineering, National University of Singapore, Singapore 119260, Singapore

Received 30 October 2006; received in revised form 6 June 2007; accepted 27 June 2007
Available online 5 July 2007

Abstract

We investigate the applicability of an incompressible diffuse interface model for two-phase incompressible fluid flows with large viscosity and density contrasts. Diffuse-interface models have been used previously primarily for density-matched fluids, and it remains unclear to what extent such models can be used for fluids of different density, thereby potentially limiting the application of these models. In this paper, the convective Cahn–Hilliard equation and the condition that the velocity field is divergence-free are derived from the conservation law of mass of binary mixtures in a straightforward way, for fluids with large density and viscosity ratios. Differences in the equations of motion with a previously derived *quasi-incompressible model* are shown to result from the respective assumptions made regarding the relationship between the diffuse fluxes of two species. The convergence properties of the model are investigated for cases with large density ratio. Quantitative comparisons are made with results from previous studies to validate the model and its numerical implementation. Tests show that the variation in volume during the computation is of the order of machine accuracy, which is consistent with our use of a conservative discretization scheme (finite volume methods) for the Cahn–Hilliard equation. Results of the method are compared with previous work for the change in topology of rising bubbles and Rayleigh–Taylor instability. Additional results are presented for head-on droplet collision and the onset of droplet entrainment in stratified flows.

Keywords: Diffuse interface; Large density ratio; Multiphase flow; Bubbles; Rayleigh–Taylor instability; Droplet collision; Stratified flow

1. Introduction

Amongst interface tracking methods such as volume-of-fluid (VOF) [1,2], level-set (LS) [3,4] and front-tracking [5], diffuse interface (DI) methods [6–8] provide a useful alternative that does not seem to suffer from problems with either mass conservation or the accurate computation of surface tension. In DI methods, the sharp fluid-fluid interface is replaced by a narrow layer in which the fluids may mix. The concept of a diffuse

* Corresponding author. Tel.: +44 (0) 207 594 1455.
E-mail address: h.ding@imperial.ac.uk (H. Ding).

0021-9991/$ - see front matter © 2007 Elsevier Inc. All rights reserved.
doi:10.1016/j.jcp.2007.06.028

interface was proposed by van der Waals long ago [9], but it has gained popularity only in recent years as a tool for numerical simulations of two-phase flows. The resulting DI method has been used for the simulation of a wide range of two-phase flow problems including vesicle dynamics [10], Hele–Shaw flows [11], head-on droplet collision [12] and moving contact lines [13,14] (see [7] for an extensive review). Of the DI models for incompressible, immiscible two-phase flow, which is the focus of our work, Model H [15] has attracted much attention in the context of the simulation of matched-density fluids. In this model, the governing equations are the continuity and momentum equations for a divergence-free velocity field, in conjunction with the convective Cahn–Hilliard equation for the order parameter. Jacqmin [14] and the present authors [16] showed that an analysis of the flow near a moving contact line based on the H Model leads to results that are directly comparable to results of the Navier–Stokes equations with a sharp interface. Kim [17] presented a comparison of (two-dimensional) numerical results obtained from the H Model for density-matched fluids with analytical results from the Navier–Stokes equations with a sharp interface for a capillary wave, and for a deformed droplet in a shear flow.

The issue whether the H Model can be applied to two-phase flows with a density contrast has received little attention, but is obviously crucial in applications. A straightforward extension of the H model would be to replace the constant density ρ_0 with a variable density $\rho(C)$ and to continue to take the velocity field to be divergence-free. This so-called *modified H Model* would be an appealing computational method for general two-phase flows, primarily because of the smooth variation of the order parameter across interfaces. It has been used previously by Jacqmin [6], for the simulation of Rayleigh–Taylor instability as well as for flows with moving contact lines [14,16,18]. Test cases using this model for fluids with a large density contrast are rare, however. An exception is a case run by Kim [17], who primarily tested his new surface tension formulation, but a detailed comparison with previous work was not provided and this single test was only qualitative. One of the main aims of the present paper is therefore to perform extensive numerical tests for a variety of problems.

In addition to the performance of the modified H model in numerical validation tests, the theoretical basis of the model for flows of fluids with a density contrast is unclear at present. Most rigorous work to justify the use of the modified H Model has focused on the stresses arising from gradients in the order parameter, with emphasis on showing that these strictly dissipate energy [6]. But a full derivation of these equations of motion is not available, to our knowledge. Jacqmin [14] merely stated that this is the simplest possible Navier–Stokes–Cahn–Hilliard DI model, and that effects of compressibility are neglected in this model. This is also borne out by more rigorous derivations of DI models for fluids with a density contrast, as these do not recover the (modified) H model. Antanovskii [19] derived a quasi-incompressible DI model for binary mixtures, wherein the immiscible liquids can mutually penetrate into each other in such a way that the sum of the *mass diffusive flow rates* of the two fluids equals zero (as discussed in more detail in the next section). As a result he obtained the conventional compressible continuity equation

$$\rho_t + \nabla \cdot (\rho \mathbf{u}) = 0, \tag{1}$$

such that the velocity field is only solenoidal if the bulk densities are equal. Lowengrub and Truskinovsky [20] extended Antanovskii's model by presenting a new formulation of the chemical potential, in which the kinetic fluid pressure and fluid density were introduced. An important issue here is that, in order for results of DI simulations to be comparable to solutions of the incompressible Navier–Stokes equations, the volume of each fluid should remain constant in time: it should not be allowed to change because of diffuse fluxes. It is anticipated that this is a concern if the velocity field is not divergence-free. A further aim of this paper is therefore to investigate the origin of the differences with the modified H Model.

We therefore first investigate in this paper the origins of the differences between the H and other DI models. In Section 2, it is shown that either the H Model or a quasi-incompressible DI model can be recovered by using different choices of definition of the diffusive fluxes. We start from the continuity equations for the binary mixtures of two fluids, and use the volume fraction of one of the fluids as the order parameter. The convective Cahn–Hilliard equation and the continuity equation for a divergence-free velocity field are then derived in a straightforward way with the assumption of incompressibility of the two-fluid mixture. Also investigated in Section 2 is whether the H Model conserves mass. Results of detailed numerical validation studies that have been carried out for various test cases are presented in Section 4. Comparisons with previous work are made

for the transition of a spherical bubble into a toroidal bubble and the nonlinear development of Rayleigh–Taylor instabilities. Mass conservation and convergence of the method are investigated in particular for rising bubbles for a very large density contrast. Finally, we apply the DI model to simulate head-on binary droplet collision to investigate the sensitivity of the results to the value of the Peclet number in the Cahn–Hilliard equation, and use the method to simulate the onset of entrainment of droplets in pressure-driven stratified flow.

2. Governing equations of motion of fluids

2.1. Continuity and Cahn–Hilliard equations

We consider here the flow of two incompressible immiscible fluids (A and B) of different density and viscosity. Similar to the VOF method, the volume fraction of one of the fluids is used to indicate the composition of the two components in a volume element in the domain. If the volume fraction of component A is denoted by C ($0 \leqslant C \leqslant 1$), the local densities of the species A and B in a volume element are

$$\tilde{\rho}_A = C\rho_A \quad \text{and} \quad \tilde{\rho}_B = (1-C)\rho_B, \tag{2}$$

respectively, where ρ_A and ρ_B denote the corresponding bulk density values. The local averaged density will be denoted by $\rho = C\rho_A + (1-C)\rho_B$.

We begin with the analysis of the conservation of mass of species A in an arbitrary volume element fixed in space. The corresponding equation of continuity can be written as

$$\frac{\partial \tilde{\rho}_A}{\partial t} + \nabla \cdot \mathbf{n}_A = 0, \tag{3}$$

where $\mathbf{n}_A$ denotes the mass flow rate (per unit volume). In the bulk region, only advection contributes to the mass flow, i.e., $\mathbf{n}_A = \tilde{\rho}_A \mathbf{u}$ where $\mathbf{u}$ is the velocity of the fluid flow, which will be defined more precisely below. In interfacial regions between the two fluids, a smooth transition of C is maintained by diffusion, and the total mass flux should include a contribution from this diffusive flow. The diffusive mass flow of component A can be expressed by $-\rho_A \mathbf{j}_A$, where $\mathbf{j}_A$ is a *volume diffusive flow rate*. Hence we have the total mass flow rate for the component A

$$\mathbf{n}_A = \tilde{\rho}_A \mathbf{u} - \rho_A \mathbf{j}_A. \tag{4}$$

Substitution of (4) in (3) gives

$$\frac{\partial \tilde{\rho}_A}{\partial t} + \nabla \cdot (\tilde{\rho}_A \mathbf{u}) - \nabla \cdot (\rho_A \mathbf{j}_A) = 0, \tag{5}$$

and a similar result can be obtained for species B. Subsequently, substitution of Eq. (2) into (5) gives

$$\frac{\partial C}{\partial t} + \nabla \cdot (\mathbf{u}C) - \nabla \cdot \mathbf{j}_A = 0 \quad \text{for component } A, \text{ and} \tag{6a}$$

similarly,

$$\frac{\partial (1-C)}{\partial t} + \nabla \cdot [(1-C)\mathbf{u}] - \nabla \cdot \mathbf{j}_B = 0 \quad \text{for component } B. \tag{6b}$$

From (6a) and (6b), we obtain

$$\frac{\mathrm{D}\rho}{\mathrm{D}t} + \rho \nabla \cdot \mathbf{u} = \nabla \cdot (\rho_A \mathbf{j}_A + \rho_B \mathbf{j}_B), \tag{7a}$$

and

$$\nabla \cdot \mathbf{u} = \nabla \cdot (\mathbf{j}_A + \mathbf{j}_B). \tag{7b}$$

In [19], Antanovskii required that the mass diffusive flows satisfy $\rho_A \mathbf{j}_A = -\rho_B \mathbf{j}_B$; evidently, this leads to Eq. (1). Hence $\mathbf{u}$ is defined in that work as the mass-averaged velocity, i.e., such that $\rho\mathbf{u} = \mathbf{n}_A + \mathbf{n}_B$, which logically

connects with the velocity used in the Navier–Stokes equations. On the other hand, the CH equation is not exactly recovered in [19] and, more importantly, if the bulk densities are not matched, the volume diffusive flow rates differ, and the total volume occupied by each fluid is no longer expected to be conserved, as is normally required in incompressible flows of immiscible fluids. Insisting on conservation of volume during the mixing process leads therefore to a different result. In this case, when an amount of fluid A flows out of an infinitesimal volume element due to interfacial diffusion, there will also be an amount of fluid B of the same volume that would enter the volume element at the same time, and vice versa. That is to say

$$\mathbf{j}_B = -\mathbf{j}_A. \tag{8}$$

This is in the spirit of the Cahn–Hilliard model for binary fluids, i.e., the diffusive flow is not related to the densities but the local compositions of the two components. We note that in this case, the alternative definition $\mathbf{u} = \mathbf{n}_A/\rho_A + \mathbf{n}_B/\rho_B$, which can be interpreted as a volume-averaged velocity, leads to the equivalent result (8). Note that the volume-averaged and mass-averaged velocities are actually the same in the bulk flow, where the diffuse flux vanishes. Hence the difference between (8) and Antonovskii's approach is either a difference in requirements imposed on the diffuse fluxes, or in the definition of the fluid velocity.

Eq. (8) indicates that the volume diffusive flux of the two species are of equal magnitude, but of opposite sign. It is therefore convenient to introduce the notation $\mathbf{j} = \mathbf{j}_A$ and $\mathbf{j}_B = -\mathbf{j}$. We can then obtain the continuity equation of a divergence-free velocity field from by substituting Eq. (8) into Eq. (7b)

$$\nabla \cdot \mathbf{u} = 0, \tag{9}$$

and the evolution equation for the volume fraction by substituting (9) into (6a) or (6b), i.e.,

$$\frac{\partial C}{\partial t} + \mathbf{u} \cdot \nabla C - \nabla \cdot \mathbf{j} = 0. \tag{10}$$

Eq. (10) is the convective Cahn–Hilliard equation, with the volume fraction as the order parameter. This shows that a divergence-free velocity and the convective Cahn–Hilliard equation can be derived in a straightforward manner from the continuity equation for binary fluids (Eq. (5)). We note that density and viscosity contrasts play no role in this deduction.

We conclude this section by investigating the conservation of global mass of either species, when Eq. (8) is used. By summing the continuity equations for each species (e.g. Eq. (5) for species A), and recognizing the relationship between volume diffusive flow (8), we obtain the continuity equation

$$\frac{\partial \rho}{\partial t} + \nabla \cdot (\rho \mathbf{u}) - (\rho_A - \rho_B)\nabla \cdot \mathbf{j} = 0. \tag{11}$$

When the densities match exactly, Eq. (11) simplifies to the compressible single-phase flow continuity equation,

$$\frac{\partial \rho}{\partial t} + \nabla \cdot (\rho \mathbf{u}) = 0. \tag{12}$$

For mixtures with a density contrast, the present model still conserves mass globally when appropriate boundary conditions are used. Let Ω be a region in two- or three-dimensional space, $\partial\Omega$ its boundary, and $\mathbf{n}$ denote the unit outward normal defined at points of $\partial\Omega$. After integrating this equation over Ω, and upon using the divergence theorem, we have

$$\int_\Omega \frac{\partial \rho}{\partial t}\, dV + \int_{\partial\Omega} \rho \mathbf{u} \cdot \mathbf{n}\, dS + (\rho_A - \rho_B) \int_{\partial\Omega} \mathbf{n} \cdot \mathbf{j}\, dS = 0. \tag{13}$$

The total mass of the whole system will be conserved, if there is no volume diffusive flow through the boundaries, i.e.,

$$\mathbf{n} \cdot \mathbf{j} = 0 \tag{14}$$

and interfacial regions do not intersect with $\partial\Omega$. It should be noted that the resulting global mass conservation does not imply that the volume enclosed by any specified C contour (e.g. $C = 0.5$) remains constant. However, such mass conservation is expected to hold as well in the sharp-interface limit, wherein

both definitions of global mass become identical. This necessary requirement for global mass conservation is therefore an appropriate boundary condition for the convective Cahn–Hilliard equation. A common type of problem wherein an interfacial region intersects a boundary is that which involves moving contact lines [14]. In such flows, however, the velocity normal to the wall is zero, and again enforcing Eq. (14) is required for global mass conservation. Finally, we note here that it is highly beneficial to use a conservative discretization scheme (e.g. finite volume methods) for Eqs. (10) or (11), in order for mass conservation to be achieved at a discrete level.

2.2. Momentum equation

We seek solutions of the modified Navier–Stokes equations

$$\rho\left(\frac{\partial \mathbf{u}}{\partial t}+\mathbf{u}\cdot\nabla\mathbf{u}\right)=-\nabla p+\nabla\cdot[\mu(\nabla\mathbf{u}+\nabla\mathbf{u}^{\mathrm{T}})]+\mathbf{f}, \tag{15}$$

where the symbol $\mathbf{f}$ denotes the body and surface forces, such as the gravity $\mathbf{g}$ and surface tension force per unit volume $\mathbf{f}_{\mathrm{st}}$. This momentum balance has been widely used in DI models [14,17–20]. When the fluids are of equal density, the results of Antanovskii [19] would indicate that Eqs. (9) and (10) can be used in conjunction with Eq. (15). We observe from Section 2.1 that in this case, the volume-averaged and mass-averaged velocities are identical, and there would be no cause for confusion as to which velocity to use in Eq. (15). For flows with a density contrast, the approach adopted by Antanovskii [19] and Lowengrub and Truskinovsky [20], i.e., using the mass-averaged velocity, appears to lead to Eq. (15). However, this approach does not result in a solenoidal velocity field, as discussed in the previous section and, indeed, not to the CH equation.

An attempt to combine a rigorous approach for the derivation of the Cahn–Hilliard equation for solenoidal velocity fields with that of the Navier–Stokes equations has been presented by Boyer [21], but it involves several approximations for a specific flow configuration. There are some further arguments for using Eqs. (9) and (10) when attempting to solve Eq. (15). First, when combining these equations with the Navier–Stokes equations, the resulting system is essentially a VOF formulation (since the diffuse flux is virtually zero outside the interfacial region, and the interfacial region is reduced when the grid is refined), with the important difference that the equation for the volume fraction contains a diffusive term that allows simple but accurate computation of surface tension and the use of advection techniques to track the interface evolution. Secondly, we note that the alternative approach adopted e.g. in [19], leads to a non-solenoidal velocity field, which cannot conserve the volume in the interfacial region. It is a concern that, in certain circumstances, the diffuse flux becomes relatively large. We have observed this in the topology change of the rising bubble in Section 4.2.2 below. In such events, Eq. (7b) indicates that the diffuse flux would lead to a highly distorted velocity field when the right-hand-side is not required to be zero. This is substantiated to some extent by our numerical experiments of the simulation specified in Section 4.2.2 below, wherein numerical instability was observed at the onset of the topology change when a quasi-incompressible model [19] was used. This drawback is circumvented by the modified H model, which decouples the velocity field and the diffuse fluxes in the continuity Eq. (9). Anticipating some of the results presented below, the topology change observed in Section 4.2.2 and the accompanying relatively large magnitude of the diffuse flux do not affect the comparison between the results of the H model and that of previous work using a level-set method.

For these reasons, the system of equations of motion for the incompressible two-component flows used in the following sections is

$$\nabla\cdot\mathbf{u}=0, \tag{16a}$$

$$\frac{\partial C}{\partial t}+\mathbf{u}\cdot\nabla C-\nabla\cdot\mathbf{j}=0, \tag{16b}$$

$$\rho\left(\frac{\partial \mathbf{u}}{\partial t}+\mathbf{u}\cdot\nabla\mathbf{u}\right)=-\nabla p+\nabla\cdot[\mu(\nabla\mathbf{u}+\nabla\mathbf{u}^{\mathrm{T}})]+\mathbf{f}\ \text{or} \tag{16c}$$

$$\frac{\partial(\rho\mathbf{u})}{\partial t}+\nabla\cdot(\rho\mathbf{u}\mathbf{u})=-\nabla p+\nabla\cdot[\mu(\nabla\mathbf{u}+\nabla\mathbf{u}^{\mathrm{T}})]+\mathbf{f}+(\rho_A-\rho_B)\mathbf{u}\nabla\cdot\mathbf{j}. \tag{16d}$$

2.3. Free energy and surface tension

A free energy density model for immiscible isothermal two-phase fluids [9], based on the volume fraction C and its gradient, is used here:

$$f = \frac{1}{2}\varepsilon\sigma\alpha|\nabla C|^2 + \varepsilon^{-1}\sigma\alpha\psi(C). \tag{17}$$

Here, f is the free energy per volume, σ is the coefficient of surface tension, ε is a measure of interface thickness, and $\psi(C) = \frac{1}{4}C^2(1-C)^2$ is the bulk energy density, which has minima at $C = 0$ and 1, corresponding to the two bulk fluids. The term $\frac{1}{2}\varepsilon\sigma\alpha|\nabla C|^2$ accounts for the excess free energy due to the inhomogeneous distribution of volume fraction in the interfacial region. The chemical potential ϕ defined by the variation of free energy with respect to the volume fraction C is

$$\phi = \frac{\delta F}{\delta C} = \varepsilon^{-1}\sigma\alpha\psi'(C) - \varepsilon\sigma\alpha\Delta C. \tag{18}$$

The diffusive flow rate is taken to be proportional to the gradient of the chemical potential [22,23], and can be written as,

$$\mathbf{j} = M\nabla\phi, \tag{19}$$

where $M > 0$ is the mobility. It is instructive to consider the case of a one-dimensional interface profile that is at equilibrium. There is then no diffusive flow anywhere and the interface profile can be obtained from $\phi = 0$ and Eq. (18). The one-dimensional solution of this equation (with the z-direction chosen along the gradient of C) is

$$C(z) = 0.5 + 0.5\tanh\left(\frac{z}{2\sqrt{2}\varepsilon}\right). \tag{20}$$

Since surface tension can be interpreted as the excess free energy per unit surface area [23], it follows that, for a flat interface at equilibrium,

$$\sigma = \varepsilon\sigma\alpha\int_{-\infty}^{+\infty}\left(\frac{\mathrm{d}C}{\mathrm{d}z}\right)^2\mathrm{d}z. \tag{21}$$

Thus, we need to set $\alpha = 6\sqrt{2}$ in Eq. (18). Finally, the surface tension force in the momentum equation can then be written as (see [6,24])

$$\mathbf{f}_{\mathrm{st}} = \phi\nabla C. \tag{22}$$

2.4. Dimensionless form

We use here the macroscopic properties of fluid A to define the two-phase flow configuration and the dimensionless parameters. Similar to the density (see the discussion just below Eq. (2)), the viscosity is approximated by $\mu = C\mu_A + (1-C)\mu_B$. Thus, the dimensionless density and viscosity are

$$\bar{\rho} = \rho/\rho_A = C + (1-C)\lambda_\rho \tag{23a}$$

$$\bar{\mu} = \mu/\mu_A = C + (1-C)\lambda_\mu \tag{23b}$$

where the density ratio and viscosity ratio are $\lambda_\rho = \rho_B/\rho_A$ and $\lambda_\mu = \mu_B/\mu_A$, respectively. For simplicity, we shall drop the overline decoration in ρ and μ below. Other dimensionless parameters are: a Reynolds number $Re = \rho_A LU/\mu_A$, capillary number $Ca = \mu_A U/\sigma$ and Bond number $Bo = \rho_A gL^2/\sigma$, where L is a global characteristic length scale and U is a characteristic velocity. Additional parameters in the DI method are a Peclet number $Pe = LU/(M_c\phi_c)$, and a Cahn number $Cn = \varepsilon/L$, where M_c and ϕ_c are the characteristic values of mobility and chemical potential. The resulting dimensionless equations of motion are

$$\nabla \cdot \mathbf{u} = 0, \tag{24a}$$

$$\frac{\partial C}{\partial t} + \mathbf{u} \cdot \nabla C - \frac{1}{Pe} \nabla \cdot (M \nabla \phi) = 0, \tag{24b}$$

$$\rho \left[\frac{\partial \mathbf{u}}{\partial t} + \mathbf{u} \cdot \nabla \mathbf{u} \right] = -\nabla p + \frac{1}{\mathrm{Re}} \nabla \cdot [\mu (\nabla \mathbf{u} + \nabla \mathbf{u}^{\mathrm{T}})] + \bar{\mathbf{f}}, \tag{24c}$$

where the mobility depends on the volume fraction through $M(C) = C(1 - C)$. The final term $\bar{\mathbf{f}}$ represents dimensionless body and interfacial forces. In the simulations reported below that involve rising bubbles, $\bar{\mathbf{f}} = \frac{\phi \nabla C}{Bo} - \vec{\mathbf{j}}$, where $\vec{\mathbf{j}}$ represents the vertical direction; in the droplet entrainment simulation reported at the end of the paper, $\bar{\mathbf{f}} = \frac{\phi \nabla C}{\mathrm{ReCa}}$.

3. Numerical methodology

A staggered grid is used for the finite-volume discretization of Eqs. (24a)–(24c). Scalar variables (pressure and volume fraction) are defined at the center of each cell while velocity components are defined at the cell faces. A two-dimensional staggered grid is shown in Fig. 1; the three-dimensional grid used in some of the simulations is a straightforward extension. Because the interfacial motion is strongly coupled with the velocity field evolution, it is important to solve the CH and NS equations in a temporally matched manner. In order to achieve this, we complete computations in the following order, here from time step n to $n + 1$:

(1) Update the volume fraction field by solving the Cahn–Hilliard Eq. (24b) with the velocity field at timestep n;
(2) Compute the surface tension force in the interfacial region, i.e., Eq. (22), at timestep $n + 1/2$ by using the averaged C value of timestep n and $n + 1$;
(3) Update the velocity field to timestep $n + 1$ by solving the momentum Eq. (24c) and continuity Eq. (24a).

In Sections 3.1 and 3.2 below, steps (1) and (3) are described.

3.1. Cahn–Hilliard equation

The numerical solution of the Cahn–Hilliard equation is complicated by the fact that it is a nonlinear fourth-order partial differential equation. Several methods for the solution of this equation have been proposed previously [8,12,17]. To remove the numerical instability due to the variable mobility and the time step constraint that arises from the fourth-order diffusion term, the split semi-implicit discretization [8] has been used in the simulations reported in this paper. This method is described in details in Ref. [8]; we briefly summarize it here. C at time t^{n+1} (denoted here by C^{n+1}) is calculated from

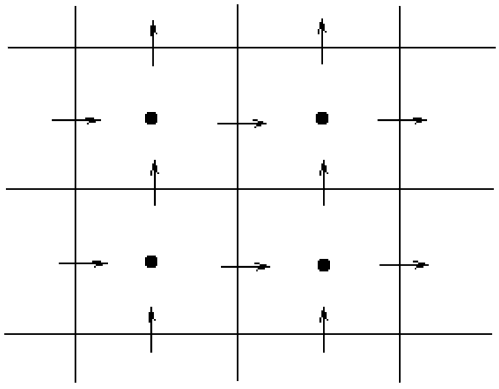

Fig. 1. Two-dimensional staggered grid on which flow variables are defined: ↑, vertical component of velocity; →, horizontal component of velocity; •, scalar variables (pressure and volume fraction).

$$\frac{\frac{3}{2}C^{n+1}-2C^{n}+\frac{1}{2}C^{n-1}}{\Delta t}=\frac{1}{Pe}(a_1\nabla^2 C^{n+1}-a_2\nabla^4 C^{n+1})+[2A(C^n,\mathbf{u}^n)-A(C^{n-1},\mathbf{u}^{n-1})] \tag{25}$$

where

$$A(C,\mathbf{u})=\frac{1}{Pe}[\nabla\cdot(M\nabla\phi)-(a_1\nabla^2 C-a_2\nabla^4 C)]-\nabla\cdot(\mathbf{u}C). \tag{26}$$

The two constants a_1 and a_2 are the approximate/optimal values related to the nonlinear mobility, and $\Delta t=t^{n+1}-t^n$ is the time step. Standard central finite difference schemes are used for the spatial discretization of the Laplacian operator in the diffusion terms.

The advection term in the Cahn–Hilliard equation (the last term on the LHS of Eq. (26)) is discretized by an upwinding finite volume scheme. More precisely, the fluxes at the cell faces are evaluated with a fifth-order weighted essentially non-oscillatory (WENO) scheme [25], using the flow velocity as the upwind direction. The use of upwinding schemes here is suggested by the advecting nature of the convective Cahn–Hilliard equation: the O(1) advection term generally plays a dominant role in the interfacial evolution (compared to the $O(\varepsilon/L_c)$ volume diffuse fluxes), except in regions with high interfacial curvature or where singularities such as break-up and coalescence occur (i.e., in regions where $L_c\sim\varepsilon$, where L_c is the radius of the curvature). Therefore, also given the shock-like profile of C across the interface, it is preferred that the local variation is dependent on conditions upstream only, as achieved by the present high-order upwinding scheme. The upwinding scheme significantly surpresses the over- and under-shoots of C profile across the interface that are normally experienced when using a central scheme.

3.2. Momentum equation

The coupling of the momentum equation and continuity equation is achieved by using a standard projection method, which is summarized as follows. First, a viscous solve is performed, using Adams–Bashforth for the advective term and Crank–Nicolson for the viscous term, resulting in an intermediate velocity $\mathbf{u}^*$:

$$\frac{\mathbf{u}^*-\mathbf{u}^n}{\Delta t}=\frac{1}{\rho^{n+1/2}}\left\{-\left[\frac{3}{2}H(\mathbf{u}^n)-\frac{1}{2}H(\mathbf{u}^{n-1})\right]+\frac{1}{2Re}[L(\mathbf{u}^*,\mu^{n+1})+L(\mathbf{u}^n,\mu^n)]\right\}, \tag{27}$$

where H denotes the discrete convection operator and L the discrete diffusion operator. The intermediate velocity $\mathbf{u}^*$ is corrected according to

$$\frac{\mathbf{u}^{n+1}-\mathbf{u}^*}{\Delta t}=-\frac{\nabla p^{n+1/2}}{\rho^{n+1/2}}. \tag{28}$$

The pressure is obtained from the requirement that the velocity field at time step $n+1$ is divergence-free constraint, i.e.,

$$\nabla\cdot\left(\frac{\nabla p^{n+1/2}}{\rho^{n+1/2}}\right)=\frac{\nabla\cdot\mathbf{u}^*}{\Delta t}. \tag{29}$$

All spatial discretizations in this subsection are central finite difference schemes.

4. Results and discussion

Two cases are considered here to validate and investigate the performance of the present DI model in simulations with a density contrast: the transition of a spherical into a toroidal rising bubble, and Rayleigh–Taylor instability. The test case of a rising bubble is first used to investigate the convergence and mass conservation properties of the method. We also apply the DI model to some other problems of interest – coalescence of binary droplets (with the specific aim to investigate the effect of the value of the Peclet number) and the onset of entrainment of droplets in stratified flows. Unless otherwise mentioned, we use the Peclet number $Pe=2/\varepsilon$ in these simulations.

4.1. Convergence and mass conservation tests

We first test the convergence and mass conservation properties of the method by simulating (in an axisymmetrical domain) a rising bubble with a large viscosity and density ratio ($\lambda_\mu = \mu_g/\mu_l = 0.01$ and $\lambda_\rho = \rho_g/\rho_l = 0.001$). The initial configuration is similar to the one shown in Fig. 2, but the size of the domain is different ($2R \times 4R$) and the initial location of the bubble is set to $1.6R$ (from the bubble center to the bottom wall), where R is the initial radius of the bubble and is defined as the unit length. Slip and non-penetration boundary conditions are enforced at all four boundaries. The Bond number $Bo(=\rho_l g R^2/\sigma)$ and Reynolds number $Re(=\rho_l g^{1/2} R^{3/2}/\mu_l)$ based on the properties of the surrounding liquid are 200 and 100, respectively. The computation stops at the dimensionless time $t = 1$ using a fixed time step that is small enough to satisfy numerical stability requirements, on four grids ($N \times 2N$): 40×80, 80×160, 160×320 and 320×640. In one set of simulations, the value of the Cahn number is fixed ($Cn = 0.01$). In a second case, the value of Cn is varied such that ε is proportional to the grid size ($\varepsilon = 0.5h$), and consequently the Cahn numbers are 0.025, 0.0125, 0.00625 and 0.003125 on the four grids, respectively. In the latter case, we have also computed the corresponding results on intermediate grids 60×120, 120×240, 240×480, such that $Cn = 0.0333$, 0.0167 and 0.00833, respectively (known hereafter as the extra set of grids).

In Figs. 3 and 4, we show a qualitative comparison of the shape of the bubble obtained from different grids by plotting the contour $C = 0.5$ at time $t = 1$. It is seen that successively refined grids result only in small differences. A first quantitative comparison between results from different grids can be made by determining the velocity at the top of the bubble at $t = 1$. When Cn is fixed, the velocity is 0.67030, 0.68088, 0.67897 and 0.67824, respectively on the successively refined grids; when Cn is varied as discussed above, the values are 0.6893, (0.6864), 0.6819, (0.6794), 0.6773, (0.6767) and 0.6756 respectively, where the solutions on the extra set of grids are included in parenthesis. Compared to the finest mesh in each set of simulations, the corresponding averaged convergence rates are approximately 1.9 and 1.7, respectively. These convergence rates are only for a single point in the flow, however.

A comparison between successively refined grids involving entire fields, in the absence of an analytical solution, can be made by computing

$$E_N(\cdot,t) = \frac{1}{\Omega}\int_\Omega |(\cdot)_N(\mathbf{x},t) - (\cdot)_{N/2}(\mathbf{x},t)|\,\mathrm{d}V \approx \frac{1}{\Omega}\sum_{i=1,j=1}^{N/2,N} |[(\cdot)_N(\mathbf{x}_{2i-1,2j-1},t) + (\cdot)_N(\mathbf{x}_{2i-1,2j},t) + (\cdot)_N(\mathbf{x}_{2i,2j-1},t) + (\cdot)_N(\mathbf{x}_{2i,2j},t)]/4 - (\cdot)_{N/2}(\mathbf{x}_{i,j},t)|h_{N/2}^2,$$

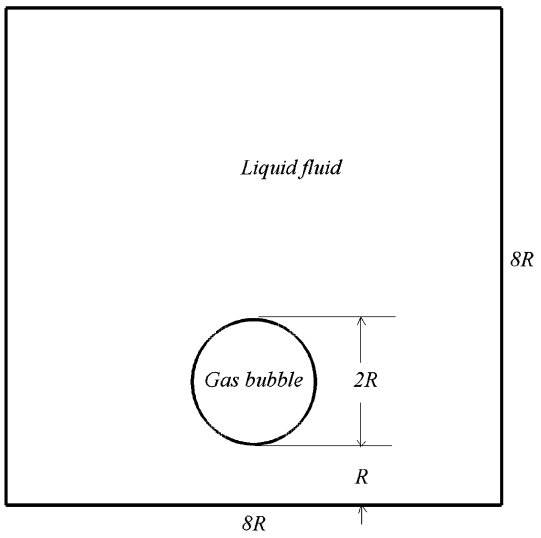

Fig. 2. Problem definition sketch for the simulation of a rising bubble. Values of fluid properties are stated in the main text.

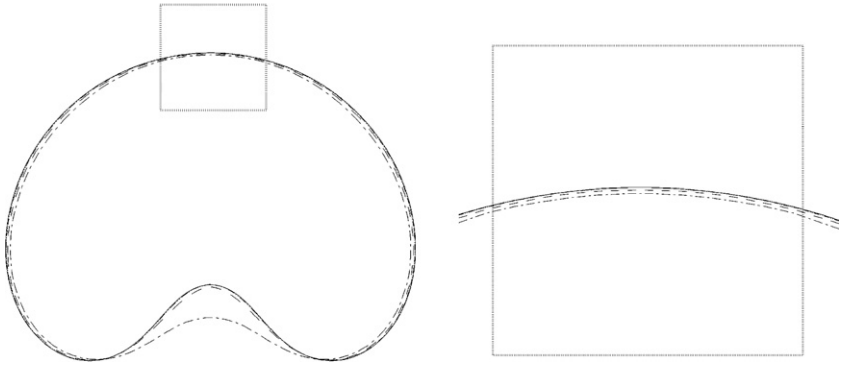

Fig. 3. Comparison of the instantaneous shape of a bubble (see Fig. 2) at $t = 1$ using a variable Cahn number as explained in the main text. Dash-dotted line denotes the solution on a 40×80 grid, dashed line the solution on a 80×160 grid, the dash–dot-dotted line represents the solution on a 160×320 and solid line the solution on 320×640 grid. The difference between solutions on the grids of 320×640 and 160×320 is indistinguishable.

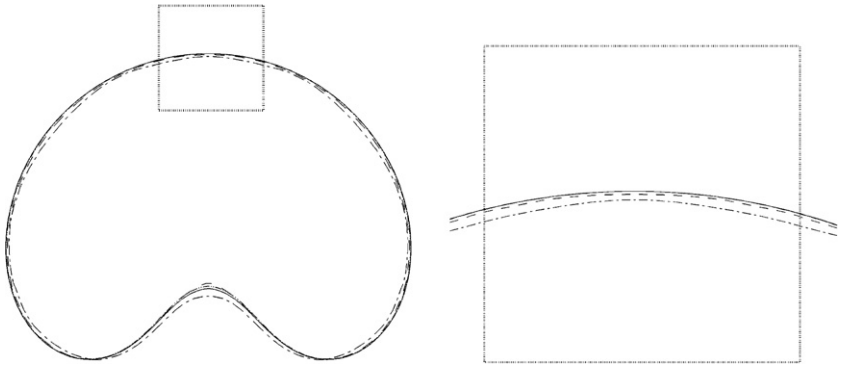

Fig. 4. As Fig. 3 but for a fixed value of the Cahn number.

where $(\cdot)_{N/2}(\mathbf{x}_{i,j},t)$ denotes the solution of a variable at the cell center $\mathbf{x}_{i,j}$ on the grid $(N/2 \times N)$ at time t, and $h_{N/2}$ represents the mesh size of the grid $(N/2 \times N)$.

Results of these convergence studies for the volume fraction C and the velocity components are given in Tables 1 and 2. The corresponding results for the convergence rate $\log_2(E_N/E_{2N})$ are also presented. The convergence rates for the volume fraction are 1.2 on the set of coarse grids: 40×80, 80×160 and 160×320, and 1.0 on the set of fine grids: 80×160, 160×320 and 320×640. They are approximately 0.8 on the set of coarse grids and 2.3 on the set of fine grids for velocity components. The relatively low convergence rates observed at coarse grids is arguably due to the value of the Cahn number and the number of grid points across the interface. On the 40×80 grid, the case studied in Table 1 corresponds to an interfacial thickness of $0.18R$, and the coarsest grid in Table 2 corresponds to only three grid points are used to resolve the interface. Since further mesh refinement would be desirable but require an excessive computational effort, we supplement the results for the (most practically relevant) case of a variable Cahn number by using the extra grids mentioned above, of which the resolutions are between the coarse and fine set of grids. The results are listed in Table 1. The convergence rate for the volume fraction is 0.78, and around 2.8 for velocity components. Since these additional data are for intermediate grid sizes compared to those discussed above, it appears that these convergence rates oscillates around second-order accuracy for the velocity components and first-order for the volume fraction when the grid is refined.

Mass conservation is naturally an important issue in numerical simulations of multiphase flows. To check the mass conservation properties of the present model, we have recorded the volume of the rising bubble at regular time intervals. The bubble volume is computed by $\int_\Omega 2\pi r(1 - C)\,\mathrm{d}A \approx \sum_{i=1,j=1}^{N,2N} 2\pi r_i(1 - C_{ij})h^2$, where

Table 1
Convergence study using a variable Cahn number

Grids	C		u_z		u_r	
	$E_N(C)$	$\log_2(E_N/E_{2N})$	$E_N(u_z)$	$\log_2(E_N/E_{2N})$	$E_N(u_r)$	$\log_2(E_N/E_{2N})$
40×80	0.0592	1.18	0.0731	0.83	0.0526	0.82
80×160	0.0262		0.0412		0.0298	
160×320	0.0128	1.04	0.00902	2.19	0.00552	2.43
60×120	0.0406	0.78	0.0788	2.76	0.0636	2.88
120×240	0.0236		0.0116		0.00731	

Details of the test cases are given in the text.

Table 2
Convergence study using a fixed Cahn number

Grids	C		u_z		u_r	
	$E_N(C)$	$\log_2(E_N/E_{2N})$	$E_N(u_z)$	$\log_2(E_N/E_{2N})$	$E_N(u_r)$	$\log_2(E_N/E_{2N})$
40×80	0.0124	2.02	0.0349	0.72	0.0187	0.79
80×160	0.00307		0.0212		0.0108	
160×320	0.00116	1.41	0.00373	2.50	0.00241	2.17

Details of the test cases are given in the text.

r denotes the radial coordinate, and C here represents the volume fraction of the liquid fluids surrounding the bubble. We have found that the changes in volume are always of the order of machine accuracy in double precision during the computation. It is not very surprising to have such a good mass conservation in this model since we solve the Cahn–Hilliard equation in conservative form using a conservative discretization scheme (finite volume method); the model does not have any non-conservative step in advancing the interface as, for instance, the reinitialization/redistance step in level-set methods. As a result, the total volume of each phase is conserved accurately, and hence the global mass. We re-emphasize here however that this volume conservation does not imply that the volume enclosed by any specified C contour (e.g. $C = 0.5$) remains constant; in fact, that is only expected to hold for $\varepsilon \to 0$.

4.2. Validation and applications

4.2.1. Rayleigh–Taylor instability

Rayleigh–Taylor instability would occur for any perturbation along the interface between a heavy fluid (A) on top of a lighter fluid (B), and is characterised by the density difference between the two fluids. The density difference is represented by the *Atwood ratio* $At = (\rho_A - \rho_B)/(\rho_A + \rho_B)$. The initial growth and long-time evolution of Rayleigh–Taylor instability has been investigated by Tryggvason [26] for inviscid incompressible flows with zero surface tension, at $At = 0.50$. Guermond et al [27] studied this stability problem at the same value of At but accounted for viscous effects. We validate our code here by investigating the same problem as Guermond et al [27], i.e., at $At = 0.50$ and Re $(=\rho_A\, d^{3/2} g^{1/2}/\mu) = 3000$, with the initial interface being located in a rectangular domain $[0, d] \times [0, 4d]$ at $y(x) = 2d + 0.1d\cos(2\pi x/d)$, which represents a planar interface superimposed by a perturbation of wave number $k = 1$ and amplitude $0.1d$. In the present case of zero surface tension, the Cahn–Hilliard equation simply amounts to interface tracking only. Computations are carried out on a 200×800 grid, the Cahn number is proportional to the mesh size h as $Cn = 0.3h = 0.0015$ and the time-step Δt is set to 0.00035. Results are presented in Fig. 5, in terms of the y-coordinate of the top of the rising fluid and the bottom of the falling fluid, together with the corresponding previous results of Tryggvason [26] and Guermond et al [27]. Good agreement is observed with these results. The evolution of the interface is shown in Fig. 6 at dimensionless times $t = 0, 1, 1.25, 1.5, 1.75, 2, 2.25, 2.5$, in which the rolling-up of the falling fluid can be clearly seen. At the early time, two counter-rotating vortices are formed along the sides of the falling filament and grow with time. To a certain extent, the two vortices are shed and a pair of secondary

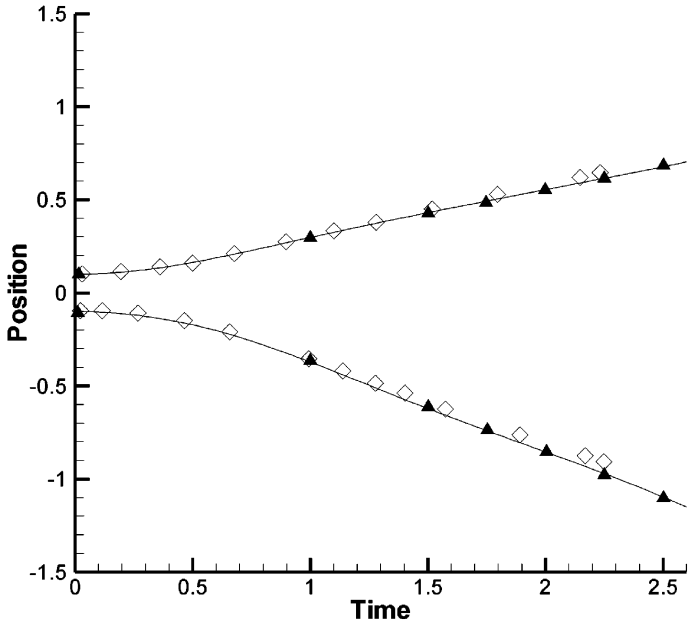

Fig. 5. The y-coordinate of the tip of the falling and rising fluid versus time: solid line denotes the present solution, the open diamonds represents the solution of Tryggvason [26] and the filled triangles that of Guermond et al. [27].

vortices occurs at the tails of the roll-ups. This interesting nonlinear evolution has been investigated numerically by many researchers [26–29]. The interfacial patterns obtained in this work appear to compare well with those in [26,27].

4.2.2. Axisymmetrical rising bubble

We revisit here the test case of the axisymmetrical rising bubble of Section 4.1, in order to compare with previous work [31] to validate the model. The configuration is shown in Fig. 2, and the properties of the fluids here are the same as the convergence tests in Section 4.1. The simulation is conducted on a grid 201×401 and the Cahn number Cn is set to 0.007. At late times the bubble evolves into a toroid (this change of topology is investigated in more detail in [30]). Our numerical simulation shows that the bubble breaks up at $t = 1.61$, and the topology change occurs at the top of the bubble, more precisely at $y = 4.09R$. These are in very good agreement with the results of Sussman and Smereka [31], who obtained $t = 1.60$ and $y = 4.05R$, respectively. The shape of the bubble at $t = 1.6$ is represented in Fig. 7 by the contour $C = 0.5$, which almost matches exactly with the result from Ref. [31] presented on the right of the figure. The instantaneous shapes of the bubble at times $t = 0, 0.2, 0.4, 0.6, 0.8, 1, 1.2, 1.4, 1.6, 1.8, 2, 2.2, 2.4, 2.6, 2.8$ and 3 are shown in Fig. 8. They also agree well with the results in Ref. [31].

4.2.3. Head-on collision and coalescence of binary droplets; effect of Pe

We consider here the application of the model for interfacial interaction, i.e., coalescence, by simulating the head-on collision of binary droplets at large density ratios. The density ratio λ_ρ and viscosity ratio λ_μ between the droplets and the ambient fluid are 1000 and 100, respectively. The dimensionless numbers are the Weber number $We = \rho\, U^2 R/\sigma$ and the Reynolds number $Re = \rho UR/\mu$, where R is the initial radius of the droplet and U is the relative velocity of the droplets at collision. In the present study, the Weber and Reynolds number are set to 16 and 50, respectively.

Simulations of the axisymmetrical binary droplet collision were carried out in a domain (2×8) on a 101×401 mesh. Slip and no-penetration boundary conditions are imposed at all boundaries of the computational domain, except for the symmetry axis. Both droplets is resolved, i.e., symmetry is not imposed between the two droplets. The droplets are initially located side by side at a center-to-centre distance of $4R$, and then

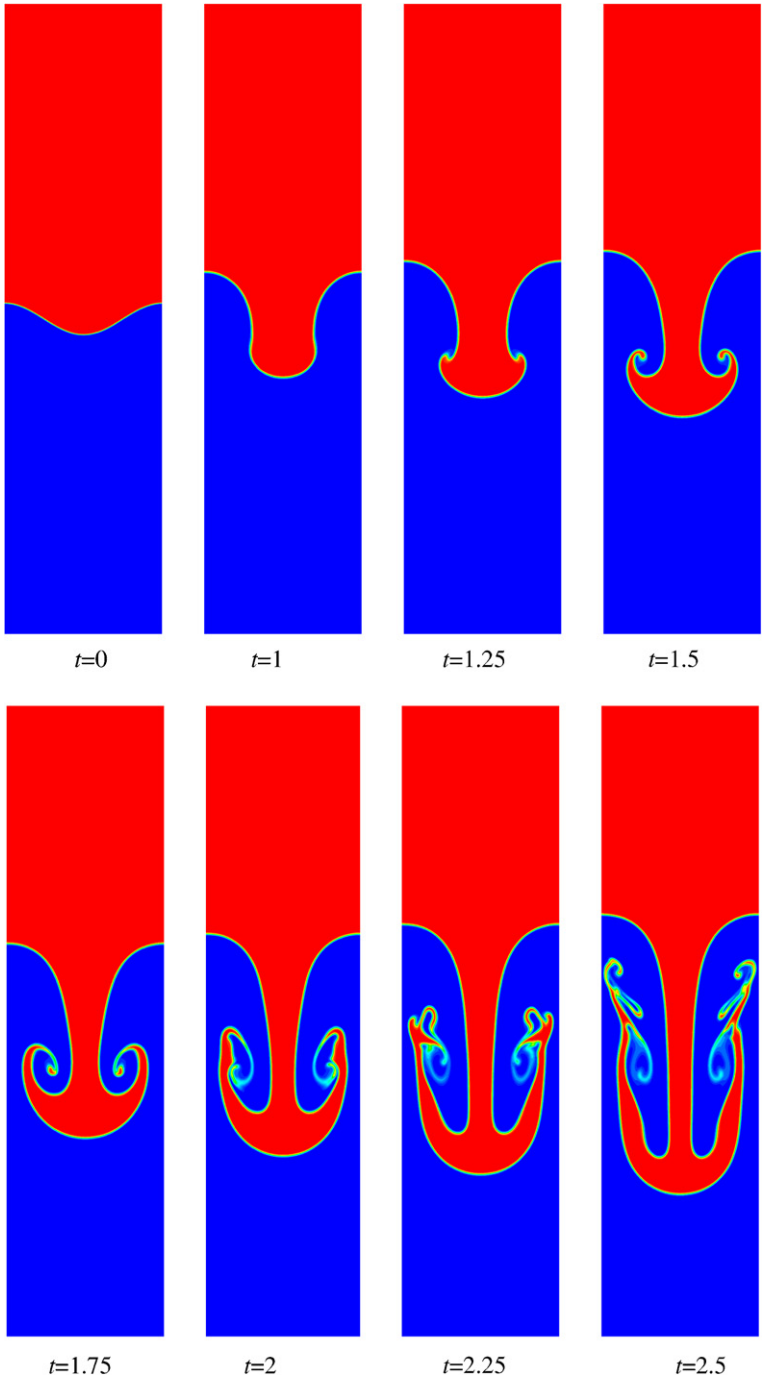

Fig. 6. Rayleigh–Taylor instability simulation at different times.

accelerated by an attractive force until collision occurs. The magnitude of the force was chosen such that the impact velocity is approximately equal to U. The simulations were conducted on a personal computer with an Intel Pentium D (dual core) CPU 3.40 GHz and 2G RAM. The time step Δt was set to $0.0008T$ and the program was run up to time $24T$, where $T = R/U$. It took a CPU time of approximately 3 h to complete this simulation.

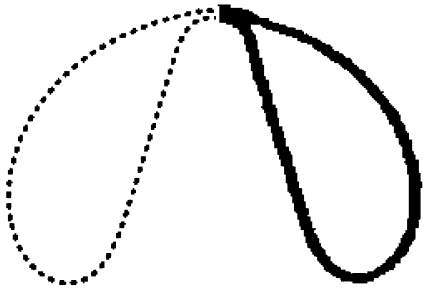

Fig. 7. Comparison of bubble shape with previous work at time $t = 1.6$. Dashed line denotes present result and solid line denotes the result from Sussman et al. [31].

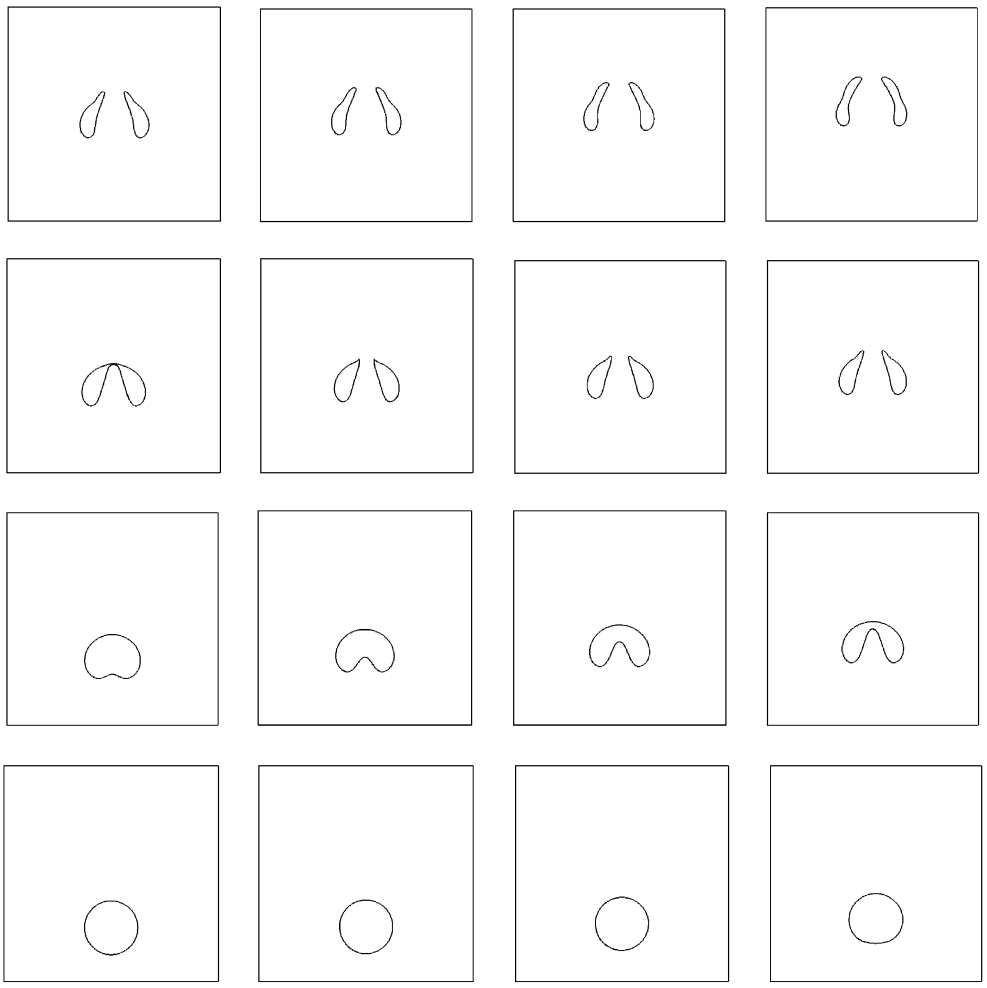

Fig. 8. Interface shapes of the bubble at time $t = 0, 0.2, 0.4, 0.6, 0.8, 1, 1.2, 1.4, 1.6, 1.8, 2, 2.2, 2.4, 2.6, 2.8$ and 3 (from left to right and from bottom to top).

The results are presented in Fig. 9 for two different values of the dimensionless mobility parameter *Pe*. The mobility parameter, which relates the rate of advection of the fluid flow to the rate of interfacial diffusion, is expected to influence results of simulations of coalescence. For a careful selection of the value of the mobility,

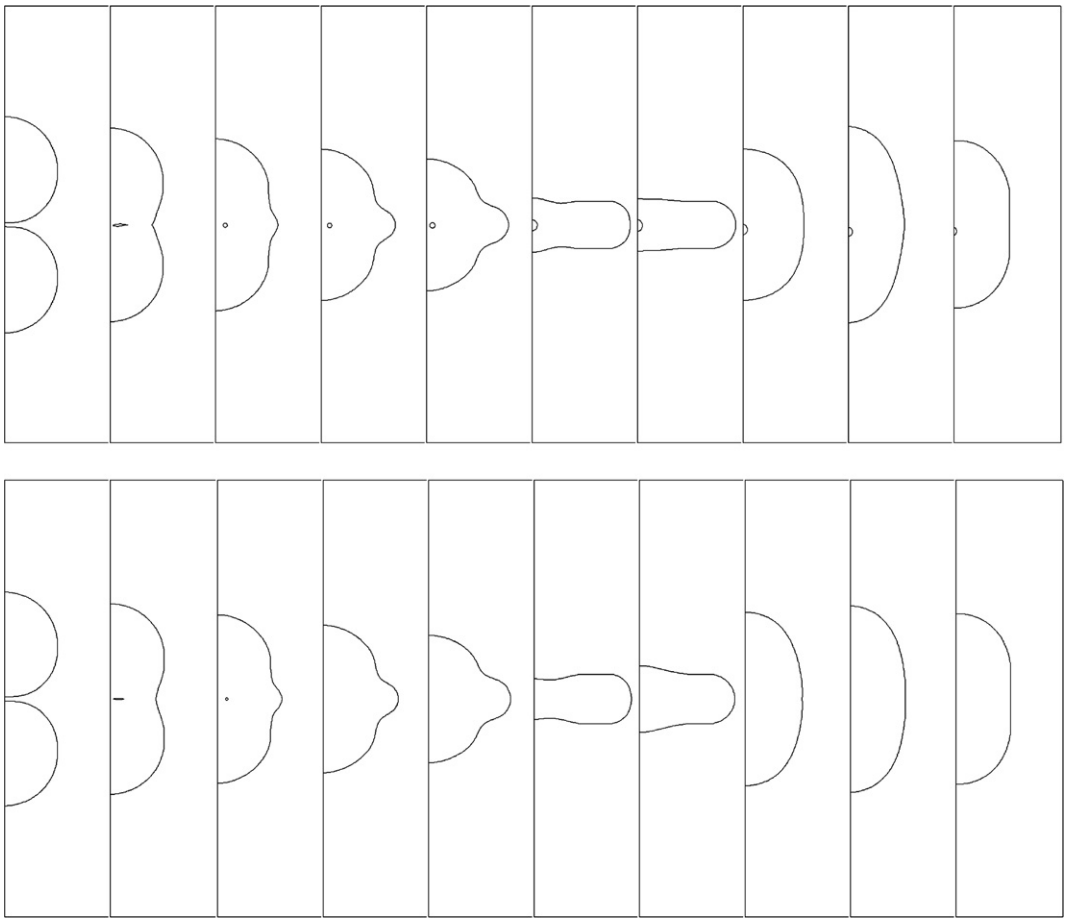

Fig. 9. Evolution of interface shapes for the head-on collision of droplets at times $t = 0, 0.4, 0.8, 1.2, 1.6, 3.6, 5.6, 9.6, 13.6$ and 20 (from left to right). The upper results are for a value of the Peclet number $Pe = 4/\varepsilon$, the lower results are for $Pe = 1/\varepsilon$.

Jacqmin [6] suggested that it must be asymptotically small when the thickness of the diffuse interface approaches zero, e.g. $M \propto \varepsilon^{\delta}$ where $1 \leqslant \delta < 2$, based on the analysis of the scales in the phase field flow physics. In Fig. 9, the effect of the value of Pe on a head-on collision is investigated, by comparing the results for $Pe = 1/\varepsilon$ and $4/\varepsilon$. In Fig. 9, we show the instantaneous shape of the collided droplets ($C = 0.5$ contours) at different times after the impact. It is interesting to observe that a tiny toroidal bubble has been trapped at the center of the coalesced droplet. In the case of the higher value of Pe, we can clearly observe how the toroidal bubble gradually becomes spherical. However, because the radius of the tiny bubble is comparable to the thickness of the diffuse interface, the volume inside the contour of $C = 0.5$ becomes smaller and smaller with time, hence a thinner interface (through mesh refinement to ensure that $\varepsilon \ll R$, where R is the radius of the bubble) would be needed to improve the simulations in this respect. We also see in the final frames that the eventual single droplet has undergone a slight unphysical displacement off the centerline (it has been verified that this displacement is reduced upon grid refinement). In the case of the lower value of Pe, the small bubble disappears even before it can become spherical. The reason for this is that diffuse fluxes are then relatively large compared and thus dissolves the tiny bubble in a short time after the collision.

4.2.4. Onset of droplet entrainment

Finally, we consider a possible application of the method: pressure-driven stratified Poiseuille flow in a 3D channel, where a lighter fluid shears over a heavier fluid. The onset of droplet entrainment is observed, resulting from the evolution of a small disturbance to the interface. The density and viscosity ratio λ_ρ and λ_μ

between the heavier and lighter fluids are both set to 10; the Reynolds number and capillary number in terms of the flow properties of the lighter fluid are set to 100 and 1, respectively. The pressure drop in the channel is unity. The simulation is performed on a $161 \times 41 \times 161$ grid, corresponding to a domain of size $1 \times 0.25 \times 1$.

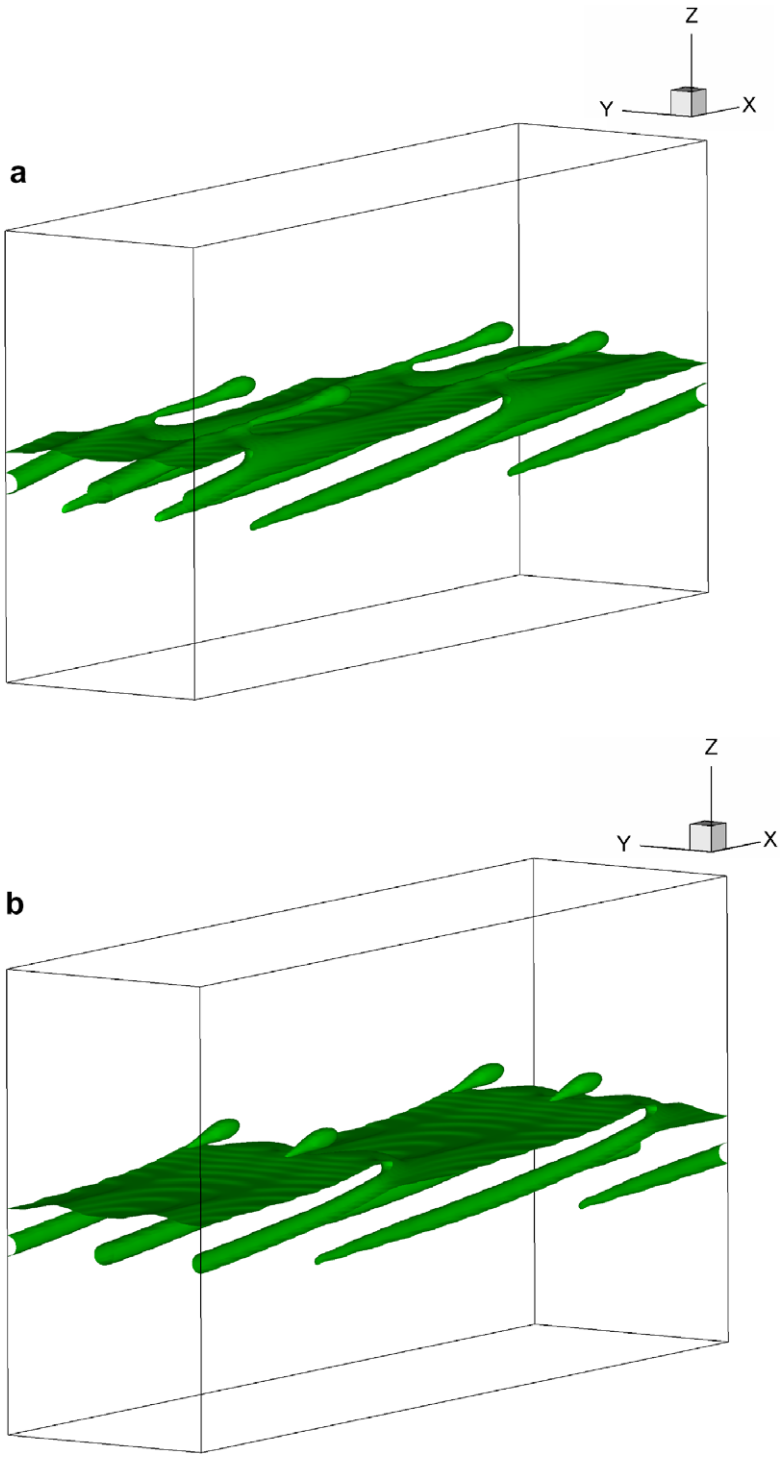

Fig. 10. Onset of droplet entrainment in stratified flow at $Re = 100$ and $Ca = 1$ (a) at the moment breakup occurring (b) at a later time.

Periodic boundary conditions are enforced in the streamwise and transverse directions. Initially, the interface is located at $z = 0.5$, i.e., halfway the channel height, and transverse and streamwise waves are superimposed. The interface shape is

$$s(z) = 0.5 + a_1 \cos(2\pi k_1 x) + a_2 \cos(2\pi k_2 y). \tag{30}$$

where x represents the streamwise direction and y the transverse direction. We choose here $a_1 = 0.075$, $a_2 = 0.1$, $k_1 = 1$ and $k_2 = 4$. The initial velocity field is the analytical uni-directional flow

$$U(z) = \begin{cases} -50[z^2 - 1 - m(z-1)], \\ -50(z^2 - mz)/\lambda_\mu, \end{cases} \tag{31}$$

where $m = (0.5 + 1.5\lambda_\mu)/(1 + \lambda_\mu)$.

The simulation results show that the wave crests are greatly elongated by the base flow (31). Eventually liquid droplets and gas bubbles are formed at the tip of the elongated interfaces. A snapshot of the simulation at the moment of droplet formation is shown in Fig. 10a. The onset of droplet entrainment can be clearly observed at the wave crests. Similarly, the troughs of the waves evolve into an elongated shape, and it is expected that these will break up at a later time into bubbles. A snapshot at a later time is shown in Fig. 10b, wherein the liquid droplets formed above the interface and longer gas troughs below the interface are noticeable.

5. Conclusion

We have investigated the applicability of diffuse interface model, specifically the so-called modified H Model, for numerical simulations of incompressible two-phase flows of fluids with a large density ratio. All the modelling issues are addressed in the framework of binary mixtures, and on the assumption that the volume diffusive flows between the two phases are only dependent on the composition–not the density. As a result, it follows that the velocity field is divergence free and the Cahn–Hilliard equation (with the volume fraction as the order parameter) can be derived in a straightforward manner from the continuity equation, regardless of the density ratio of the fluids. We have also shown that the global volume can be conserved, which has also been confirmed by numerical tests. Numerical simulations show that the model can be applied to a wide range of two-phase problems with large density and viscosity ratio, such as the topology change of bubbles and the coalescence of binary droplets, and to industrial applications such as oilfield-related pipe flow.

Specific advantages of the DI method are that it can accurately conserve global mass, and is relatively easy to implement. On the other hand, it requires rather many grid points to achieve a smooth variation of dependent variables in a sufficiently narrow interfacial region. This restricts the ability of DI methods in resolving small interfacial structures, e.g. to a scale comparable to the interface thickness, which is comparatively larger than its counterparts (VOF and LS) on the same grid.

References

[1] C.W. Hirt, B.D. Nichols, Volume of fluid (VOF) method for the dynamics of free boundaries, J. Comput. Phys. 39 (1981) 201–225.
[2] B.D. Nichols, C.W. Hirt, R.S. Hotchkiss, SOLA-VOF: A solution algorithm for transient fluid flow with multiple free boundaries, Los Alamos National Lab Report LA-8355, 1980.
[3] M. Sussman, P. Smereka, S. Osher, A level set approach for computing solutions to incompressible two-phase flow, J. Comput. Phys. 114 (1994) 146–159.
[4] D. Adalsteinsson, J. Sethian, A fast level set method for propagating interfaces, J. Comput. Phys. 118 (1995) 269–277.
[5] G. Tryggvason, B. Bunner, A. Esmaeeli, et al., A front-tracking method for the computations of multiphase flow, J. Comput. Phys. 169 (2001) 708–759.
[6] D. Jacqmin, Calculation of two-phase Navier–Stokes flows using phase-field modelling, J. Comput. Phys. 155 (1999) 96–127.
[7] D.M. Anderson, G.B. McFadden, A. A Wheeler, Diffuse-interface methods in fluid mechanics, Ann. Rev. Fluid Mech. 30 (1998) 139–165.
[8] V.E. Badalassi, H.D. Ceniceros, S. Banerjee, Computation of multiphase systems with phase field models, J. Comput. Phys. 190 (2003) 371–397.
[9] J.D. van der Waals, Verhandel. Konink. Akad. Weten. AmsterdamSect vol. 1 No. 8 (Dutch) 1893, Translation of J.D. van der Waals (The thermodynamic theory of capillarity under the hypothesis of a continuous density variation) J. Stat. Phys. (1979).

[10] T. Biben, K. Kassner, C. Misbah, Phase-field approach to three-dimensional vesicle dynamics, Phys. Rev. E 72 (2005) 041921.
[11] R. Folch, J. Casademunt, A. Hernández-Machado, L. Ramirez-Piscina, Phase-field model for Hele–Shaw flows with arbitrary viscosity contrast. I. Theoretical approach, Phys. Rev. E 60 (1999) 1724.
[12] P. Yue, J.J. Feng, C. Liu, J. Shen, A diffuse-interface method for simulating two-phase flows of complex fluids, J. Fluid Mech. 515 (2004) 293–317.
[13] P. Seppecher, Moving contact lines in the Cahn–Hilliard theory, Int. J. Engng. Sci. 34 (1996) 977–992.
[14] D. Jacqmin, Contact-line dynamics of a diffuse fluid interface, J. Fluid Mech. 402 (2000) 57–88.
[15] M.E. Gurtin, D. Polignone, J. Vinals, Two-phase binary fluids and immiscible fluids described by an order parameter, Math. Models Meth. Appl. Sci. 6 (1996) 815–831.
[16] H. Ding, P.D.M. Spelt, Inertial effects in droplet spreading: a comparison between diffuse interface and level-set simulation, J. Fluid Mech. 576 (2007) 287–296.
[17] J. Kim, A continuous surface tension force formulation for diffuse-interface models, J. Comput. Phys. 204 (2005) 784–804.
[18] D. Jacqmin, Onset of wetting failure in liquid–liquid systems, J. Fluid Mech. 517 (2004) 209–228.
[19] L.K. Antanovskii, A phase field model of capillary, Phys. Fluids 7 (4) (1995) 747.
[20] J. Lowengrub, L. Truskinovsky, Quasi-incompressible Cahn–Hilliard fluids, Proc. R. Soc. London Ser. A 454 (1998) 2617–2654.
[21] F. Boyer, A theoretical and numerical model for the study of incompressible mixture flows, Comp. Fluids 31 (2002) 41–68.
[22] J.W. Cahn, J.E. Hilliard, Free energy of a nonuniform system I, J. Chem. Phys. 28 (1958) 258.
[23] J.W. Cahn, J.E. Hilliard, Free energy of a nonuniform system III, J. Chem. Phys. 31 (1959) 688.
[24] D. Jacqmin, An energy approach to the continuum surface tension method, AIAA96-0858, in: Proceedings of the 34th Aerospace Sciences Meeting and Exhibit, American Institute of Aeronautics and Astronautics, Reno, 1996.
[25] X.D. Liu, S. Osher, T. Chan, Weighted essentially non-oscillatory schemes, J. Comput. Phys. 115 (1994) 200–212.
[26] G. Tryggvason, Numerical simulations of the Rayleigh–Taylor instability, J. Comput. Phys. 75 (1988) 253–282.
[27] J.L. Guermond, L. Quartapelle, A projection FEM for variable density incompressible flows, J. Comput. Phys. 165 (2000) 167–188.
[28] B.J. Daly, Numerical study of two fluid Rayleigh–Taylor instabilities, Phys. Fluids 10 (1967) 297.
[29] X.Y. He, S.Y. Chen, R.Y. Zhang, A lattice Boltzmann scheme for incompressible multiphase flow and its application in simulation of Rayleigh–Taylor instability, J. Comput. Phys. 152 (1999) 642–663.
[30] T. Bonometti, J. Magnaudet, Transition from spherical cap to toroidal bubbles, Phys. Fluids 18 (2006) 052102.
[31] M. Sussman, P. Smereka, Axisymmetric free boundary problems, J. Fluid Mech. 341 (1997) 269–294.